



A coupled thermal/fluid/chemical/ablation method on surface ablation of charring composites



Weijie Li^a, Haiming Huang^{a,*}, Xiaoliang Xu^b

^a Institute of Engineering Mechanics, Beijing Jiaotong University, Beijing 100044, China

^b Beijing Institute of Near Space Vehicle's System Engineering, Beijing 100076, China

ARTICLE INFO

Article history:

Received 11 November 2016

Received in revised form 3 February 2017

Accepted 18 February 2017

Available online 27 February 2017

Keywords:

Surface ablation

Coupled thermal/fluid/chemical/ablation method

Charring composites

Thermal protection

ABSTRACT

The surface ablation of charring composites is critical for estimating the performance of the thermal protection system of a hypersonic vehicle during reentry. A coupled thermal/fluid/chemical/ablation method is proposed to solve the surface ablation of charring composites with the pyrolysis. Comparing to the previous method, it considers that the chemical reactions between the pyrolysis gases and the oxidative gases in the boundary layer have further influences on the oxidation of surface char in the Park's model. The new mathematical models are discretized by using the center and up-wind formats, and solved by the FORTRAN and MATLAB codes written. The numerical results indicate that the coupled method shows a validation in solving the surface ablation by comparing to the experimental data, and it can more accurately determine the surface recession rate of charring materials. This study will be helpful for the design of the thermal protection systems in hypersonic reentry vehicles.

© 2017 Elsevier Ltd. All rights reserved.

1. Introduction

Thermal protection system (TPS) is essential for safety of vehicles subjected to severe aerodynamic heating [1]. Reentry vehicles usually take charring materials as TPS materials due to their volume and surface ablation to protect the vehicles from the huge amount of heat generated by the friction of the atmosphere [2–6]. On the one hand, the researchers focused on the volume ablation process of these composites. For instance, the models for the volume ablation often used heat conduction equations considering the pyrolysis of materials to calculate the in-depth materials' thermal performances, such as the reported Li's pyrolysis interface and layer models [7–9], which could estimate the thickness of each layer during the pyrolysis. Also, the heat conduction equation combining with the Arrhenius's law served as a model for obtaining the mass flow rate of pyrolysis gases during heating [10,11]. Furthermore, the mechanisms of pyrolysis gases produced from the pyrolysis in the porous char were deeply studied by many researchers. For example, with the species mass conservation, momentum conservation expressed by Darcy's law and energy conservation for gases and solid equations, the products produced from phenol, the pressure distributions in the materials and temperatures for

both pyrolysis gases and solid could be analyzed [12,13]. Then in recent years, the thermodynamics and transport properties were determined by Mutation++ and measured using gas chromatography techniques [14,15]. On the other hand, the surface ablation is worthy for attention. It is the phenomenon that the gases in the boundary layer react with surface char accompanying with the mass loss and the surface recession. Firstly, the chemical reactions occurring at materials' surface for the oxidation of graphite under reentry conditions were usually (1) $C + O_2 \rightarrow CO + O$; (2) $C + O \rightarrow CO$; (3) $C + O + O \rightarrow C + O_2$ or (1) $C + O_2 \rightarrow CO$; (2) $C + N \rightarrow CN$; (3) $3C \rightarrow C_3$, in which the thermo-chemical and the sublimation reaction rates were based on both the kinetic theory and the experimentally determined reaction probabilities by the Knudsen-Langmuir equation [16–22]. And the well-known slow and fast reaction rates at high temperatures were proposed by Scala after reviewing the kinetic data and reaction-rate expressions by several authors [23]. Also, Maabs concluded the previous researches on the kinetic expressions for estimation of the chemical reaction rates at high temperatures and presented the temperature range of each expression [24]. Secondly, the computer program such as Charring Material Ablation which coupled with a boundary layer solver could obtain the regression of the ablation surface [25]. But this program could not easily obtain the gas generation rate in the fast decomposing materials. And STABII program took temperature dependent materials properties as well as the surface recession into account [26]. Simultaneously, the influences of the chemical

* Corresponding author.

E-mail addresses: 13115259@bjtu.edu.cn (W. Li), huanghaiming@tsinghua.org.cn (H. Huang), 12121036@bjtu.edu.cn (X. Xu).

Nomenclature

L	thickness of boundary layer [m]	ν'	stoichiometric coefficient of reactant [–]
y	spatial coordinate along the thickness direction in the inner charring material [m]	ν''	stoichiometric coefficient of product [–]
x	spatial coordinate in axial direction in the boundary layer [m]	κ	curvature radius [m]
t	time [s]	\dot{m}	mass flux rate [$\text{kg m}^{-2} \text{s}^{-1}$]
r	spatial coordinate in radial direction [m]	k	reaction rate constant
ρ	gas density [kg/m^3]	d	diameter of bore [m]
u	gas velocity/gas velocity in axial direction [m/s]	α	reaction probability [–]
p	gas pressure [Pa]	ε	emissivity of the ablation surface [–]
h	specific enthalpy [J/kg]	σ	Stefan-Boltzmann constant [$\text{W m}^{-2} \text{K}^{-4}$]
T	gas temperature [K]	q	heat flux [W/m^2]
c_p	specific heat at constant pressure [$\text{J kg}^{-1} \text{K}^{-1}$]	φ	thermal blockage coefficient [–]
G	function of density, radial velocity and radial coordinate [$\text{kg m}^{-3} \text{s}^{-1}$]	ΔH	heat of combustion [J/kg]
F	function of density and axial velocity [$\text{kg m}^{-2} \text{s}^{-1}$]	R	gas constant [$\text{J mol}^{-1} \text{K}^{-1}$]
H	eigenvalue for the radial pressure gradient [Pa/m^2]	Q	ablation heat in per area [J/m ²]
μ	dynamic viscosity [$\text{kg m}^{-1} \text{s}^{-1}$]	θ	graphite vapor pressure coefficient [–]
v	gas velocity in radial direction [m/s]	Subscripts	
λ	thermal conductivity [$\text{W m}^{-1} \text{K}^{-1}$]	C	char
Y	mass fraction [–]	w	surface
V	diffusion velocity [m/s]	$cold$	cold wall
$\dot{\omega}$	chemical reaction rate [$\text{mol m}^{-3} \text{s}^{-1}$]	r	recovery
W	molecular weight [kg/mol]	f	the position before detached normal shock wave
\bar{W}	mean molecular weight [kg/mol]	b	the position behind detached normal shock wave
C_p	molar heat capacity at constant pressure [$\text{J mol}^{-1} \text{K}^{-1}$]	k	species index
X	mole fraction [–]	i	ith reaction
$[X]$	molar concentration [mol/m^3]	s	oxygen-bearing species on the reactant side of the equation
D_{jk}	multicomponent diffusion coefficients [m^2/s]	v	vapor
D_{km}	mixture averaged diffusion coefficients [m^2/s]	g	gas
D_k^T	thermal diffusion coefficients [$\text{kg m}^{-1} \text{s}^{-1}$]		

reactions occurring in the char layer, i.e. cracking of gases and gas-solid interactions, on the surface ablation were analyzed using frozen, chemical equilibrium, or finite rate models [27]. Another significant part of numerical tools is a three dimensional Navier-Stokes code Langley Aerothermodynamic Upwind Relaxation Algorithm, which could simulate the hypersonic non-equilibrium flow over blunt bodies in order to obtain the parameters, such as pressure and species, used in the surface ablation mechanisms [28]. Finally, the arc jet test facilities in NASA Ames Research Center were built to simulate the high enthalpy aerodynamic environment and measure the materials' properties in ablation [29]. The facilities included the Aerodynamic Heating Facility (AHF), the Panel Test Facility (PTF), Interaction Heating Facility (IHF), and other support systems. On the basis of these arc jet facilities, the measured recession, thermal responses, and shape change were presented for a phenolic impregnated carbon ablator [30,31]. But the experimental methods were not applicable for the ablation due to that these ground tests were difficult to accurately simulate the actual reentry conditions. Meanwhile, the flight tests were prohibitively expensive.

In the previous researches, the way to obtain the surface recession usually takes the gas-solid interactions, the thermal responses of materials' surface and the aerodynamic properties in the boundary layer into consideration. However, the surface ablation of the charring materials is extremely complex, which relates not only with above elements but also with the chemical performances in the boundary layer, like the kinds of the interactions between the pyrolysis gases which inject to materials' surface with the oxidative gases in the boundary layer, the production and consumption of oxidative gases near the materials' surface, the reac-

tion mechanisms of the hydrocarbons [32,33]. In this respect, a coupled thermal/fluid/chemical/ablation method is proposed in this paper to estimate the surface recession more accurately.

2. Model

2.1. Physical model

With the surface of charring materials suffering heating, in the inner ablator, the composite is divided into three layers, namely the virgin layer, the pyrolysis layer and the char layer. In the outer ablator adjacent to the material's surface, there is an ablation layer. The detail physical and chemical phenomena in each layer can be seen in Refs. [7–9]. In the mean time, the pyrolysis gases produced in the pyrolysis layer flow to the materials' surface and inject to the boundary layer. In this boundary layer, the pyrolysis gases which are usually hydrocarbons react with the oxidative gas species in the inflow, which form a counterflow diffusion flame. The reactions of above gases affect the aerodynamic performances near the composite's surface, such as the mole fractions, the species and the molecular weights of gases. Using these chemical performances as well as the aerodynamic parameters, the oxidation of surface char occurs. The physical model coupled with the thermal transport in the inner materials, the gases reactions in the boundary layer and the oxidation of surface char built in this paper can be seen in Fig. 1.

In Fig. 1, L represents the thickness of the boundary layer. If x and r denote the independent spatial coordinates in the axial and the radial directions, respectively, the material surface is located

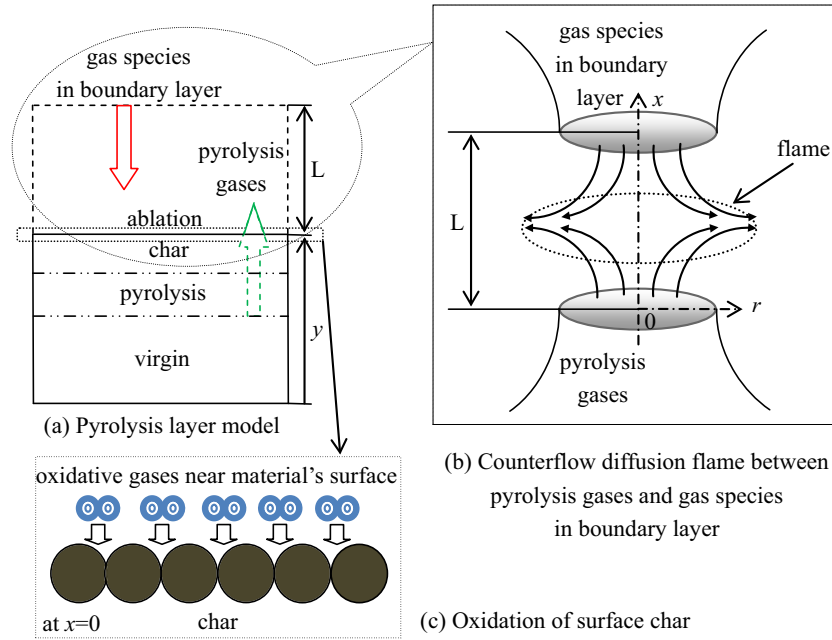


Fig. 1. Schematic diagram of coupled thermal/fluid/chemical/ablation model.

at $x = 0$ and the detached normal shock wave is located at $x = L$. At $x = 0$, the pyrolysis gases flow toward the positive x direction due to the pressure in the materials is higher than that in the aerodynamic environment. At $x = L$, the species in the inflow flow toward the negative x direction. In Fig. 1(c), the double-circles and each circular represent the oxidative gas species near the material's surface and the surface char.

2.2. Mathematical models

2.2.1. Pyrolysis layer model

The thermal transport in the inner materials has to be solved by building the pyrolysis layer model with the major assumptions [34]:

- (a) The pyrolysis gases do not react chemically with the porous char layer through which it flows.
- (b) There is no secondary cracking of pyrolysis gases.

The nonlinear transient heat conduction equations of charring materials with moving interfaces can be seen in Refs. [7–9].

Especially, it is necessary to write the surface energy balance equation here since that it is important in building the bridge between the coupled thermal/fluid/chemical/ablation performances.

$$-\lambda_c \frac{\partial T}{\partial y} = \varphi q - \varepsilon \sigma T_w^4 + \dot{m}_c \Delta H_c \quad (1)$$

where λ is the thermal conductivity, T is the temperature, y is the coordinate along the thickness direction, ε is the emissivity of the ablation surface, σ is Stefan-Boltzmann constant and \dot{m} is the mass flux, ΔH is the heat of combustion. The subscript w and C represent the surface of the ablator and the surface char. And thermal blockage coefficient φ is a number between 0 and 1 relating with mass injection rate, recovery enthalpy and cold wall heat flux q_{cold} , which can be written as

$$\varphi = 1 - 0.58(\dot{m}_{g,w} + \dot{m}_c) \frac{h_r}{q_{cold}} \quad (2)$$

where h is the enthalpy. The subscripts g and r represent the gases and recovery. h_r is a function with the gases' enthalpy and velocity at the boundary edge.

$$h_r = h_b + \frac{u_b^2}{2} \quad (3)$$

where u is the gases' velocity. The subscript b represents the boundary edge, which is seen as the position behind the detached normal shock wave.

And the hot wall heat flux q is given

$$q = q_{cold} \left(1 - \frac{h_w}{h_r} \right) \quad (4)$$

where the wall enthalpy h_w can be seen as a temperature dependent function (see in Refs. [7–9]).

The mass flux of surface char can be calculated on the basis of the mass conservation as

$$\dot{m}_c = \rho_c \frac{dy_w}{dt} \quad (5)$$

where ρ is the density, t is the time point and dy_w/dt is the surface recession rate.

In addition, the normal velocity u_w of pyrolysis gases at the materials' surface can be calculated on the basis of the ideal gas equation.

$$u_w = \frac{\dot{m}_g R T_w}{p_b \bar{W}_w} \quad (6)$$

where R is the gas constant, p is the pressure and \bar{W} is the mean molecular weight of gases.

Thus, the thermal responses of charring materials, such as the surface temperature and the velocity of pyrolysis gases at the materials' surface, can be obtained based on the equations in this part. These two parameters are closely tied to the fluid and chemical analysis of the boundary layer by Eq. (1), in which the right terms respectively relate with the aerodynamic and fluid performances of the boundary layer, the thermal responses of the composites, and the chemical and ablation performances on the material's surface.

2.2.2. Fluid model at stagnation line

Due to the fact that the ablation problem considered in this paper is at the stagnation line, the mass, the momentum and the energy conservation equation of the detached normal shock wave can be adopted to obtain the fluid performances in the boundary edge. The conservation equations are

$$\rho_f u_f = \rho_b u_b \quad (7)$$

$$p_f + \rho_f u_f^2 = p_b + \rho_b u_b^2 \quad (8)$$

$$h_f + \frac{u_f^2}{2} = h_b + \frac{u_b^2}{2} \quad (9)$$

where the subscript f represents the position forward the detached normal shock wave.

The thermodynamic properties of inflow with real gas effects may be denoted by [35]

$$h = h(p, \rho) \quad (10)$$

$$T = T(p, \rho) \quad (11)$$

The specific enthalpy, pressure, gas density and gas velocity behind the detached normal shock wave, where is the edge of the boundary layer, can be obtained from Eqs. (7)–(10). Then the temperature can be expressed by Eq. (11).

Thus, the fluid performances, such as the temperature, the velocity and the pressure of the gases in the boundary layer edge, can be obtained based on the equations in this part. They are regarded as parts of boundary conditions of the model for obtaining the chemical responses in the next section.

2.2.3. Counterflow diffusion flame model in boundary layer

For a reentry vehicle with large curvature radius at the stagnation point, the inflow can be seen as homogeneous at the stagnation line. Meanwhile, the kinds of pyrolysis gases change quite little in some temperature range [36,37]. Thereby, the following simplifying assumptions of the counterflow diffusion flame can be applied to the stagnation line in the boundary layer [38]:

- The temperature and species mass fractions are functions of x alone.
- The thermodynamic pressure is constant throughout the flow field in the axial direction, but the pressure gradient term appears in the momentum equation in the radial direction.

Based on the Navier-Stokes equations in cylindrical coordinates, the physiochemical processes are expressed by the following conservation equations in the axisymmetric system

$$G - \frac{dF}{dx} = 0 \quad (12)$$

$$\frac{d}{dx} \left[\mu \frac{d}{dx} \left(\frac{G}{\rho} \right) \right] - 2 \frac{d}{dx} \left(\frac{FG}{\rho} \right) + \frac{3}{\rho} G^2 + H = 0 \quad (13)$$

$$2F c_p \frac{dT}{dx} - \frac{d}{dx} \left(\lambda \frac{dT}{dx} \right) + \sum_k \rho c_{pk} Y_k V_k \frac{dT}{dx} - \sum_k h_k \dot{\omega}_k W_k = 0 \quad (14)$$

$$2F \frac{dY_k}{dx} - \frac{d}{dx} (\rho Y_k V_k) - \dot{\omega}_k W_k = 0 \quad k = 1, 2, \dots, K \quad (15)$$

where $G(x) = -\frac{\rho v}{r}$ and $F(x) = \frac{\rho u}{2}$.

In these equations, v is the radial velocity, μ is the dynamic viscosity, Y is the mass fraction, V is the diffusion velocity, $\dot{\omega}$ is the chemical reaction rate and W is the molecular weight. The sub-

script k is the species index. In addition, H is the eigenvalue for the radial pressure gradient which is equal to the pressure at the position behind the detached normal shock wave

$$H = \frac{1}{r} \frac{\partial p}{\partial r} \equiv \text{const} \quad (16)$$

The specific heat at constant pressure c_p and thermal conductivity λ in Eq. (14) are respectively given as

$$c_p = \sum_{k=1}^K c_{pk} Y_k = \sum_{k=1}^K \frac{C_{pk}}{W_k} Y_k \quad (17)$$

$$\lambda = \frac{1}{2} \sum_{k=1}^K X_k \lambda_k + \frac{1}{\sum_{k=1}^K X_k / Y_k} \quad (18)$$

where the mean molecular weight $\bar{W} = \frac{1}{\sum_{k=1}^K Y_k / W_k}$, C_{pk} is molar heat capacity at constant pressure of k th specie, and X_k is the mole fraction of the k th specie expressed as $X_k = \frac{Y_k W}{W_k}$.

The diffusion velocity can be expressed as

$$V_k = -\frac{1}{X_k} D_{km} \frac{dX_k}{dx} - \frac{D_k^T}{\rho Y_k} \frac{1}{T} \frac{dT}{dx} \quad (19)$$

where $D_{km} = \frac{1-Y_k}{\sum_{j \neq k} X_j / D_{jk}}$ and D_{jk} , D_{km} , D_k^T are multi-component, mixture averaged and thermal diffusion coefficients, respectively.

The chemical reaction rate is a complicated parameter written as

$$\dot{\omega}_k = \sum_{i=1}^I (v_{ki}' - v_{ki}'') \left[k_{fi} \prod_{k=1}^K [X_k]^{v_{ki}'} - k_{ri} \prod_{k=1}^K [X_k]^{v_{ki}''} \right] \quad (20)$$

where v_{ki}' and v_{ki}'' are the stoichiometric coefficients of the k th reactant and product species in the i th reaction, k_f and k_r are respectively the forward and the reverse rate constant of the i th reaction, and the molar concentration of the k th species $[X_k] = \rho \frac{Y_k}{W_k}$.

The boundary conditions for the counterflow diffusion flame are

$$x = 0 : F = \rho_w u_w / 2, G = 0, T = T_w, \rho u Y_k + \rho Y_k V_k = (\rho u Y_k)_w \quad (21)$$

$$x = L : F = \rho_b u_b / 2, G = 0, T = T_b, \rho u Y_k + \rho Y_k V_k = (\rho u Y_k)_b \quad (22)$$

It is clear that these boundary conditions relate with the thermal and fluid results from Sections 2.2.1 and 2.2.2. In addition, the thickness of the boundary layer supplying the range of the diffusion flame can be expressed as [39]

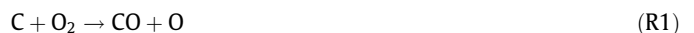
$$L = \kappa \rho_f / (\rho_f + \rho_b) \quad (23)$$

where κ is the curvature radius at the stagnation point.

By the equations in this part, the chemical responses near the materials' surface can be calculated, such as the mole fraction of O_2 and O , the mean molecular weight of gases, and the gas density.

2.2.4. Oxidation ablation model of surface char

Based on the works of Park [21,40], the oxidation reactions of surface char ablation are as follows



The reactions rates $k_{w,r}$ for above reactions are based on kinetic theory, which are

$$k_{w,r} = \alpha_r \sqrt{\frac{RT_w}{2\pi W_s}} \quad (24)$$

where α_r is the reaction probability for each of the surface reactions and W_s is the oxygen-bearing species molecular weight on the reactant side of the equation. The experimentally determined reaction probabilities are

$$\alpha_1 = \frac{1.43 \times 10^{-3} + 0.01 \exp(-1450/T_w)}{1 + 2 \times 10^{-4} \exp(13000/T_w)} \quad (25)$$

$$\alpha_2 = 0.63 \exp(-1160/T_w) \quad (26)$$

$$\alpha_3 = \alpha_2 \quad (27)$$

The mass fluxes of each species associated with reactions R1–R3 are

$$\dot{m}_{O_2} = -\rho_{O_2} k_{w,1} + \rho_O k_{w,3} \quad (28)$$

$$\dot{m}_{CO} = \frac{W_{CO}}{W_{O_2}} \rho_{O_2} k_{w,1} + \frac{W_{CO}}{W_O} \rho_O k_{w,2} \quad (29)$$

$$\dot{m}_O = \frac{W_O}{W_{O_2}} \rho_{O_2} k_{w,1} - \rho_O k_{w,2} - \rho_O k_{w,3} \quad (30)$$

The density of gas species ρ_k can be calculated by

$$\rho_k = \frac{p_b W_k}{RT_w} \quad (31)$$

It is noted that the species density in the uncoupled method is only affected by the species in the inflow. However, the species density and molecular weight near the materials' surface change when taken the combustion diffusion flame into consideration in the coupled method.

The total mass flux of surface char is by summing over all the mass fluxes above

$$\dot{m}_C = \sum_{i=1}^{ns} \dot{m}_i \quad (32)$$

where ns represent the total number of relevant species that occur between the solid char and the gases at the surface.

The solution of the equations in this part must consider the thermal, fluid and chemical results in Sections 2.2.1–2.2.3. Then the ablation response of surface char can be calculated by Eqs. (24)–(32).

3. Numerical approach

The central difference format, up-wind scheme and the Newton Secant method are taken into consideration in the numerical methods for solving the nonlinear pyrolysis layer model [8]. The equations in the fluid model are solved by the quasi-Newton method. The equations in the counterflow diffusion flame are discretized by using the central difference format for the diffusion term and the up-wind scheme for the convection term [32,33].

The uncoupled method is a way to estimate the surface recession by considering the thermal responses in the inner materials, the fluid properties in the inflow and the surface ablation mechanism of char. The coupled method makes further efforts by taking account of the gases combustion performance in the boundary besides the thermal/fluid/ablation influences. The calculation paths of these two methods are shown in Fig. 2.

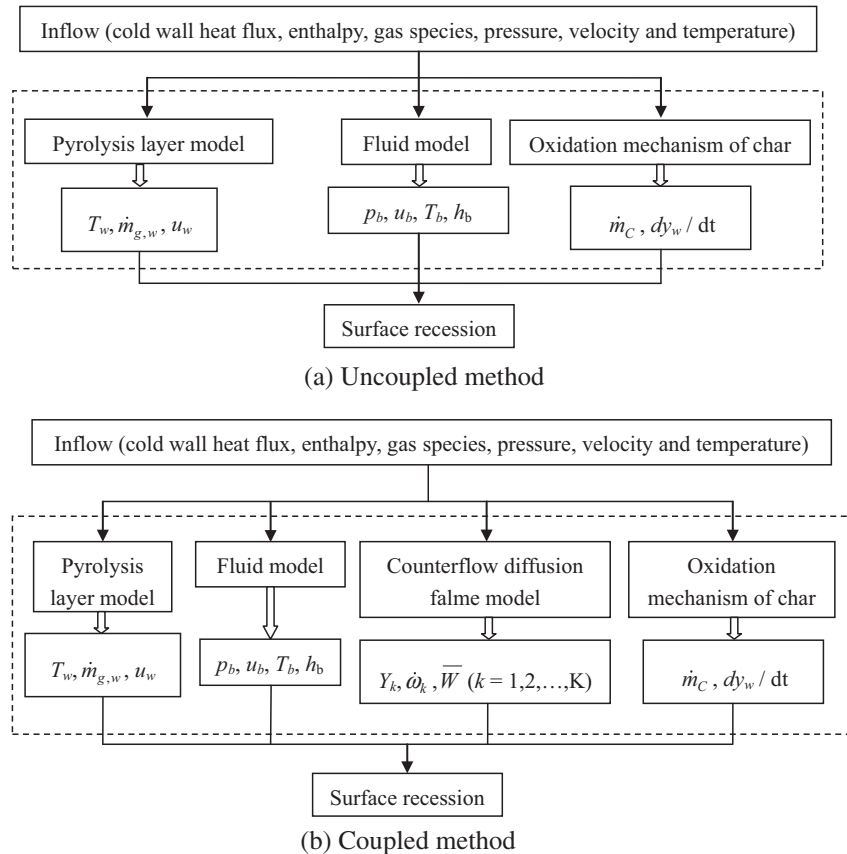


Fig. 2. Simulation methods.

4. Examples

4.1. Material properties

PICA is a low density, rigid and carbon fiber insulation impregnated composite material, which is invented at NASA Ames Research Center (ARC) in the 1990s as the heat-shield material on the reentry vehicles. The properties were measured to provide a database for researchers to use in their ablation models. The PICA's properties which have to be utilized in this paper are listed in Table 1 [31,41–45].

In addition, Table 2 gives the mole fractions of the main components of pyrolysis gases coming out of the material's surface [37].

4.2. Arcjet test conditions

The 'iso-q' shape model with a 5 cm thickness is taken account in this paper, which was used in the arcjet tests in previous researches [30]. The arcjet tests were conducted with the AHF and the IHF at NASA ARC [29,30]. In addition, the diameter of stream outlet bore is 5.99 cm in the AHF and 8 cm in the IHF. The different test conditions at the stagnation for PICA models are listed in Table 3 [30].

It should be pointed out that in Table 3, the pressure and the enthalpy could be seen as the value for p_f and h_f in Section 2.2; corresponding to the stagnation pressures, the temperature of the inflow (T_f) can be checked and is 216.65 K; the inflow gases are composed of argon and air, which concludes oxygen and nitrogen. It is widely known that the mass fraction of oxygen and nitrogen is 21% and 79% in air under this temperature. Moreover, the ratio between the oxygen mole fraction and the nitrogen mole fraction can be denoted as

$$\frac{X_{O_2}}{X_{N_2}} = \frac{Y_{O_2}}{Y_{N_2}} \frac{W_{O_2}}{W_{N_2}} \quad (33)$$

Thus the gas species in the inflow for the four tests under the experimental temperature without ionization and dissociation are calculated and listed in Table 4 [30].

The mass rate (m_f) of the inflow in Table 3 is a value corresponding to u_f , the density of the mixture gases and the diameter of stream outlet bore. Then the inflow gases' velocity can be expressed as

$$u_f = \frac{m_f}{\rho_f \left[\pi \left(\frac{d}{2} \right)^2 \right]} \quad (34)$$

where d is the diameter of stream outlet bore in AHF and IHF. On the basis of the idea gas law, ρ_f can be denoted by

$$\rho_f = \frac{p_f \bar{W}_f}{RT_f} = \frac{p_f (W_{O_2} X_{O_2} + W_{N_2} X_{N_2} + W_{Ar} X_{Ar})}{RT_f} \quad (35)$$

4.3. Measured ablation performance

The surface recessions at the stagnation point were measured using two single-wavelength pyrometers and one dual-wavelength pyrometer in arcjet tests at ARC, which could be found in Table 5 [30].

Table 4
Gas species of the inflow [30].

No. [–]	Mole fraction of O ₂ [%]	Mole fraction of N ₂ [%]	Mole fraction of Ar [%]
1	17.16	68.64	14.2
2	17.84	71.36	10.8
3	18.4	73.6	8
4	18.48	73.92	7.6

Table 5
Recession in each arcjet test [30].

No. [–]	Heating time [s]	Measured recession [mm]
1	33	2.27/2.20
	60	4.28/4.58/4.76
2	42	3.71/3.65/3.95/3.52/3.68/4.12/3.69
	60	5.21/5.23
3	34	4.61/4.43
4	30	5.41/4.97

Table 1
Material properties of PICA [31,41–45].

Name	Value	Unit	Ref.
Virgin density	274	kg/m ³	[31]
Char density	229	kg/m ³	
Commencing temperature of pyrolysis	422	K	[41]
Completing temperature of pyrolysis	1033	K	
Emissance of char	0.9	–	
Pyrolysis heat of phenolic resin	2.34×10^5	J/kg	[42]
Specific heat of pyrolysis gases	9630	J g ^{−1} K ^{−1}	
Commencing temperature of surface ablation	1242	K	[43]
Frequency factor of pyrolysis of phenolic resin	4.48×10^9	s ^{−1}	[44]
Activation energy of pyrolysis of phenolic resin	1.70×10^5	J/mol	
Order of reaction of pyrolysis of phenolic resin	3	–	
Heat of combustion of char	1.16×10^7	J/kg	[45]

Table 2
The components' mole fractions of pyrolysis gases at material surface [37].

H ₂	CH ₄	CO	H ₂ O	CO ₂	C ₂ H ₆
59.4%	14.9%	12.7%	12.7%	0.2%	0.1%

Table 3
Arcjet test conditions at NASA ARC [30].

No. [–]	Facility [–]	Heat flux [W/m ²]	Pressure [Pa]	Enthalpy [MJ/kg]	Mass rate [kg/s]	Argon fraction [%]	Time [s]
1	AHF	1.69×10^6	5000	17.8	0.2	14.2	60
2	AHF	2.46×10^6	8500	20.0	0.34	10.8	60
3	IHF	3.95×10^6	17,200	22.8	0.45	8	34
4	IHF	5.52×10^6	27,300	25.3	0.67	7.6	30

4.4. Results and discussions

In this paper, the uncoupled method to obtain the surface recession in each arcjet test deals with the equations in Sections 2.2.1, 2.2.2 and 2.2.4. It is a common method for estimating the ablative performance in many previous researches. While the coupled one considers the equations in Sections 2.2.1–2.2.4 which adds the influence of the chemical performance coming from the gases combustion in the boundary layer. Based on FORTRAN and MATLAB codes, the uncoupled and coupled ablative performances for PICA in each arcjet test can be obtained.

4.4.1. Uncoupled methods

The surface recession of PICA model in each arcjet test calculated by the uncoupled method is discussed in this Part. The measured and predicted recessions from tests and calculations are shown in Fig. 3.

In Fig. 3, the solid line represents the surface recession of PICA model in each test condition by the uncoupled calculation. The dashes are the measured recessions at different time points. And the dot is the mean measured values at different time points. It can be seen that the surface recession increases with the increasing of the heat flux at the materials' surface. The recessions calculated

by the uncoupled method are always lower than those measured ones, at least the mean measured values. However, with the increasing of the heat flux, the calculated values get close to the measured ones. It is deduced that the contents of the oxidizing gases near the materials' surface may be less than those used in the uncoupled method or the gases species may change during the heating. In conclusion, there are some defects of this uncoupled method to deal with surface recession of materials' surface.

4.4.2. Coupled methods

To improve the accuracy of estimation for the surface recession by the numerical methods, the results calculated by the coupled method are presented in this Part. Due to the counterflow diffusion flame added in the calculations, the parameters which are used in

Table 6
The parameters in the boundary layer.

No.	p_b [Pa]	L [m]	u_b [m/s]	T_b [K]
1	23122.42	0.027417	216.2085	355.0322
2	25394.83	0.032713	226.0469	296.3777
3	37111.30	0.037497	240.4155	266.7507
4	43297.89	0.042577	258.2526	243.3029

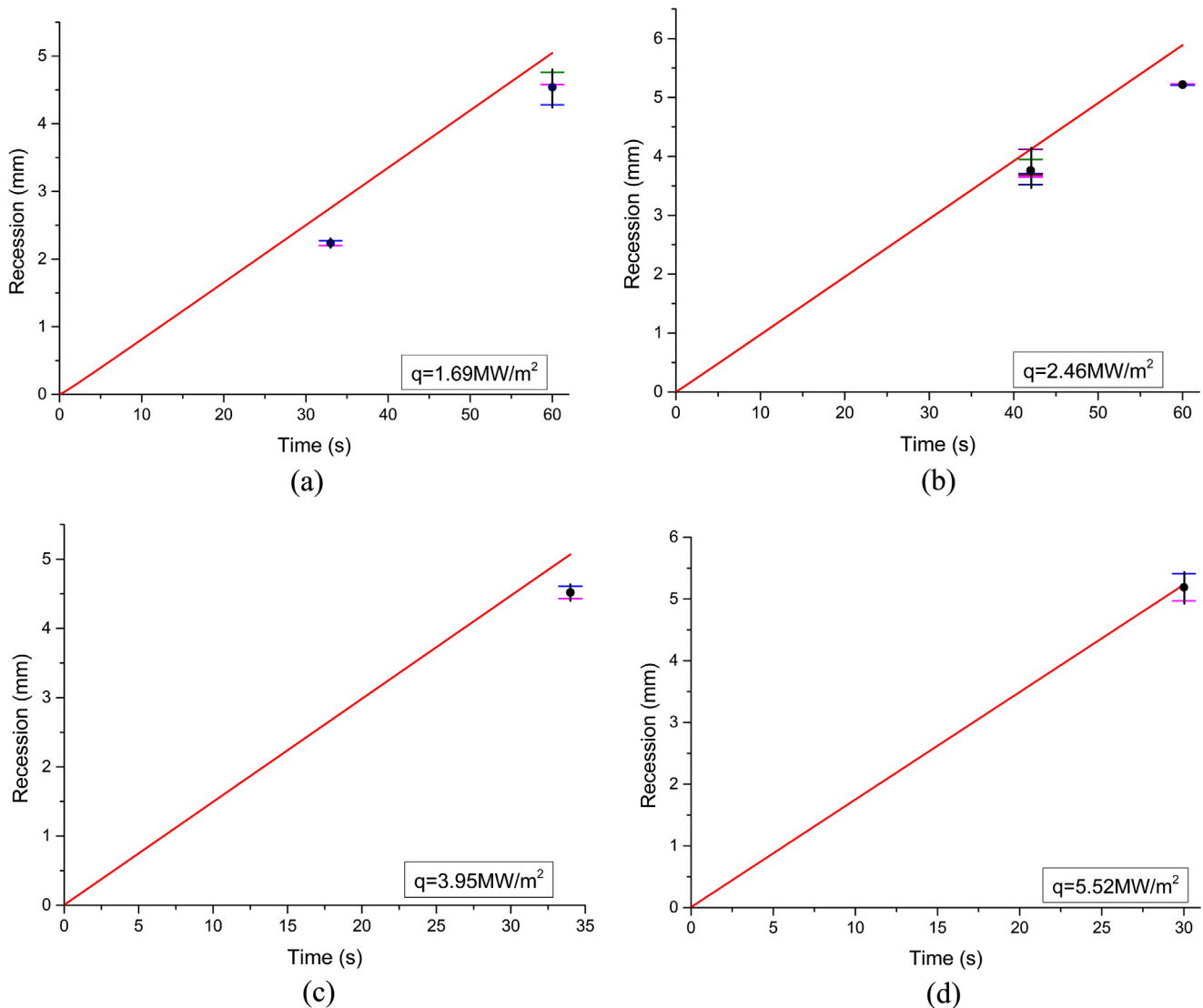


Fig. 3. Measured and predicted surface recession for (a) case 1, (b) case 2, (c) case 3, (d) case 4 using uncoupled method.

Section 2.2.3 needed to be demonstrated in Table 6 as parts of the boundary conditions of the counterflow flame model. These parameters in the boundary layer are obtained by the equations in the fluid model and Eqs. (33)–(35).

In addition, the mole fraction of gases species at the boundary layer edge can be found in Table 3. And the temperature and pyrolysis gases' velocity at material's surface are just the surface temperature calculated by the pyrolysis layer model and Eq. (6). The temperatures and pyrolysis gases' mass fluxes at the materials' surface can be seen in Figs. 4 and 5. These are the other parts of the boundary conditions for the counterflow diffusion flame model.

Simultaneously, the chemical rate expressions for 325 elementary reactions between the hydrocarbon in the pyrolysis gases and the gases species in the inflow, and the thermodynamic properties of 53 species with temperature fewer than 6000 K can be checked out in Ref. [46].

The predicted surface recessions using the coupled method in each arcjet test comparing to the measured values in Table 5 are drawn in Fig. 6.

It can be seen from Fig. 6 that at 33 s in case 1, the surface recession is respectively 2.76 mm and 2.64 mm using the uncoupled and the coupled method; the recession is respectively 2.27 mm, 2.20 mm and 2.235 mm as the maximum, the minimum and the average experimental data. The coupled method decreases the sur-

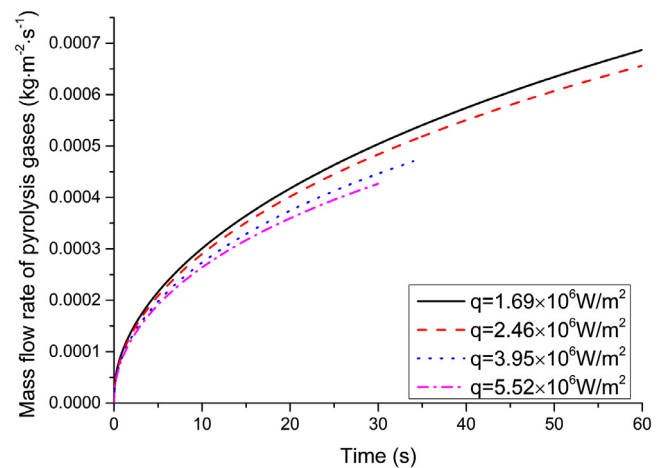


Fig. 5. Predicted pyrolysis gases' mass flux at the materials' surface.

face recession by 4.35% compared to the uncoupled method. The uncoupled results are higher than the maximum, the minimum and the average measured values by 17.75%, 20.29% and 19.02%, respectively. The coupled results are more than the three measured values by 14.02%, 16.67% and 15.34%, respectively. At 60 s in case 1,

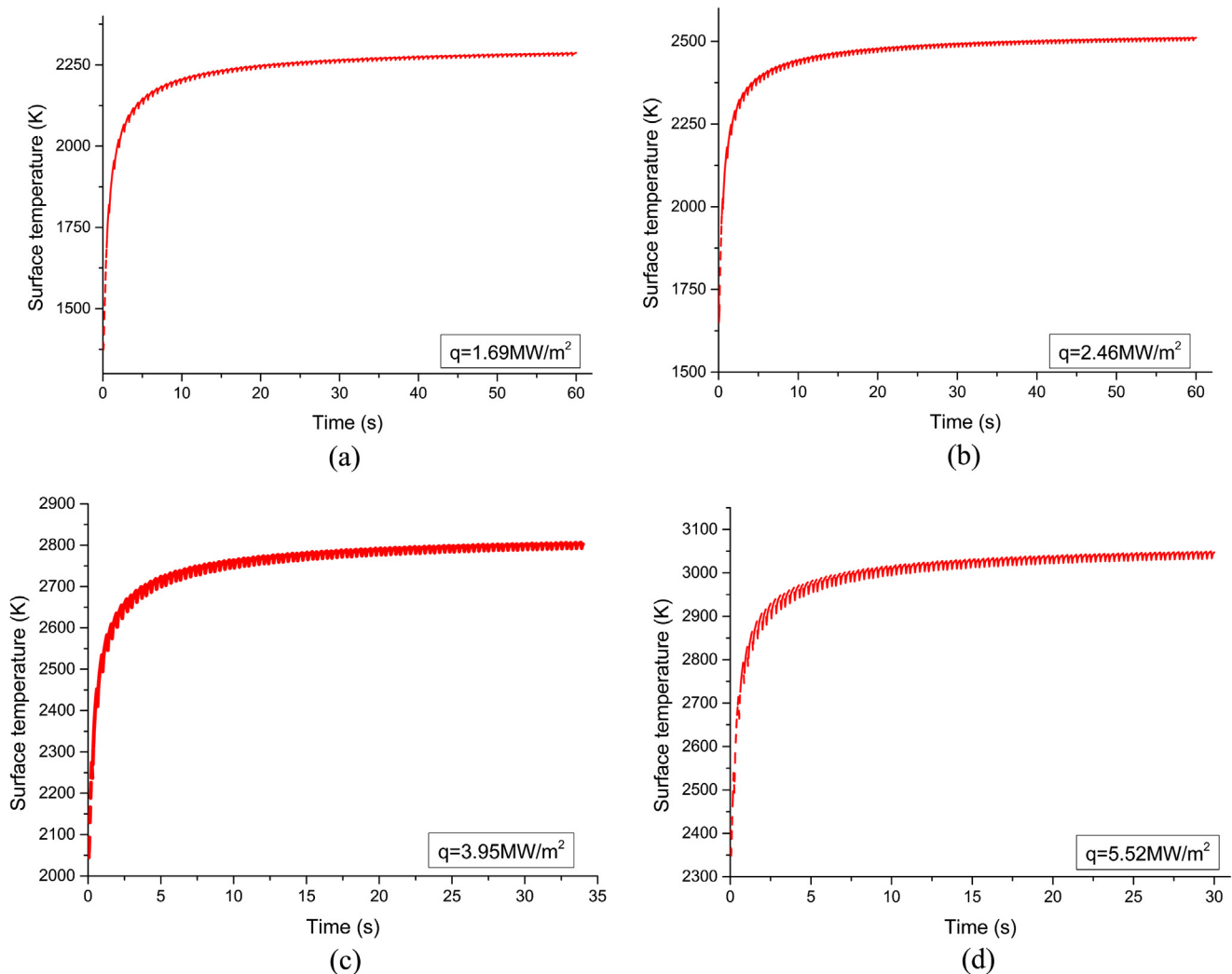


Fig. 4. Predicted surface temperature for (a) case 1, (b) case 2, (c) case 3, (d) case 4.

the coupled recession is 4.97 mm, which is more accurate than the uncoupled one (5.04 mm) by 1.39%. The uncoupled results are higher than the maximum, the minimum and the average measured values by 5.56%, 15.08% and 9.92%, respectively. The coupled results are larger than the three measured values by 4.23%, 13.88% and 8.65%, respectively. At 42 s in case 2, the surface recessions are 4.12 mm and 4.19 mm using the uncoupled and the coupled method. Comparing to the maximum, the minimum and the average measured values, the uncoupled results are more than them by 0%, 14.56% and 8.74%. And the coupled results are more than them by 1.67%, 15.99% and 10.26%. At 60 s in case 2, the surface recessions are 5.89 mm and 5.63 mm using the uncoupled method and the coupled method. The uncoupled results are larger than the maximum, the minimum and the average measured values by 11.21%, 11.54% and 11.38%. The coupled results are more than the three measured values by 7.10%, 7.46% and 7.28%. At 34 s in case 3, the surface recession is respectively 5.07 mm and 4.87 mm using the uncoupled and the coupled method. The uncoupled results are larger than the maximum, the minimum and the average measured values by 9.07%, 12.62% and 10.85%. And the coupled results are larger than the three measured values by 5.34%, 9.03% and 7.19%. At 30 s in case 4, using the uncoupled and the coupled method, the surface recessions are 5.23 mm and 5.03 mm. Both the results using the uncoupled and the coupled

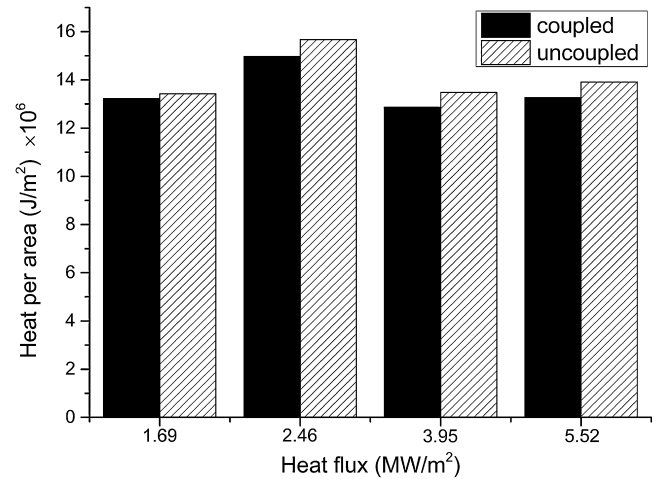


Fig. 7. Comparison of ablation heat of surface char between the coupled and the uncoupled method results.

method are larger than the minimum measured value. The uncoupled result is higher than the maximum measured value, but the coupled result is lower than the maximum measured value. All

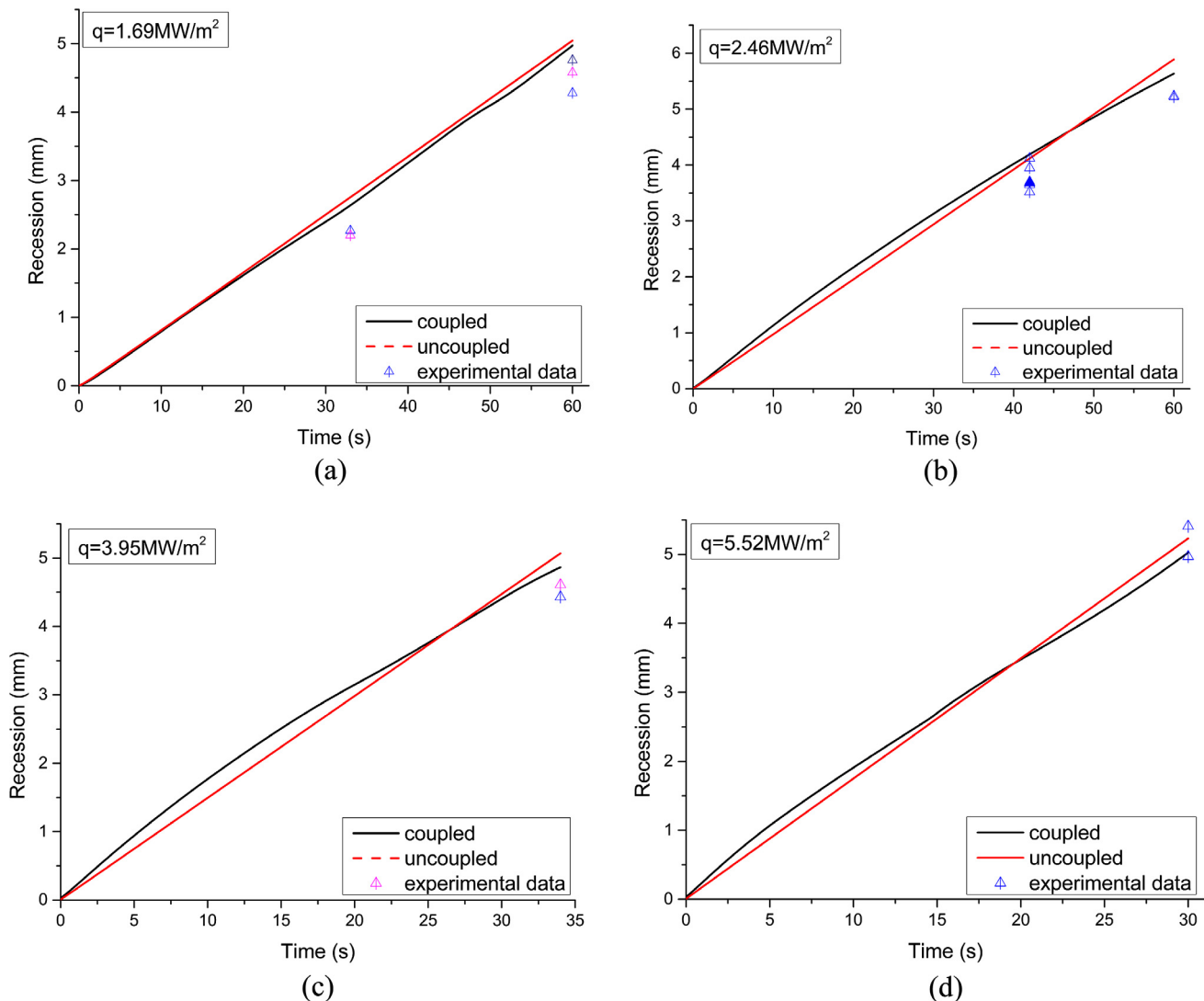


Fig. 6. Measured and predicted surface recession for (a) case 1, (b) case 2, (c) case 3, (d) case 4 using coupled method.

in all, the coupled method reduces the surface recession compared to the uncoupled method. In each case, the surface recession calculated by the coupled method increases much more rapidly than the recession calculated by the uncoupled method at the beginning. However, with heating continuing, the increasing of the coupled results becomes slow. Finally, the coupled results are less than the uncoupled results at the ending time. Furthermore, the coupled surface recession results increase with the increasing of the heat fluxes. And the coupled result gets closer to the average measured value when the heat flux rises, except the one in case 4. Generally speaking, the surface recessions calculated by the thermal/fluid/chemical/ablation method are more accurate compared to the results by the uncoupled method.

In order to compare the ablation heat during heating, Eq. (36) gives the way

$$Q_c = \int_0^{t_{tot}} \dot{m}_c \Delta H_c dt \quad (36)$$

where t_{tot} is the total heating time in each test and Q is the ablation heat in per area at the materials' surface.

Then the heat in per area of surface char during the whole heating is presented in Fig. 7 for each case using both the uncoupled and the coupled methods. The error between the coupled and the uncoupled results are respectively 1.49%, 4.46%, 7.75% and 4.32% in case 1, case 2, case 3 and case 4. It is visual that with the heat flux increasing, the decreasing of the ablation heat of surface char using the coupled method gets larger than that using the uncoupled method, except case 4. In a word, the coupled method reduces the ablation heat of surface char compared to the uncoupled method.

In addition, the influence on the surface recession from the heat flux is discussed. Fig. 8 shows the comparison of surface recession when the cold wall heat flux changes from 1.0 MW/m² to 5.0 MW/m². It can be seen clearly that the surface recession grows with the increasing of the cold wall heat flux. But the rising rate of the surface recession decreases when the cold wall heat flux rises. It demonstrates that when the heat flux is low, the reactions in the boundary layer may not completely appear. And the oxidative gases still exist in a large amount near the material's surface, which can react with the surface char leading to the surface recession. When the heat flux is high, more reactions in the boundary layer happen consuming the oxidative gases. Thus, there are limited oxidative gases reacting with the surface char. So in spite of the heat flux rises by the same amount, the increasing rate of the sur-

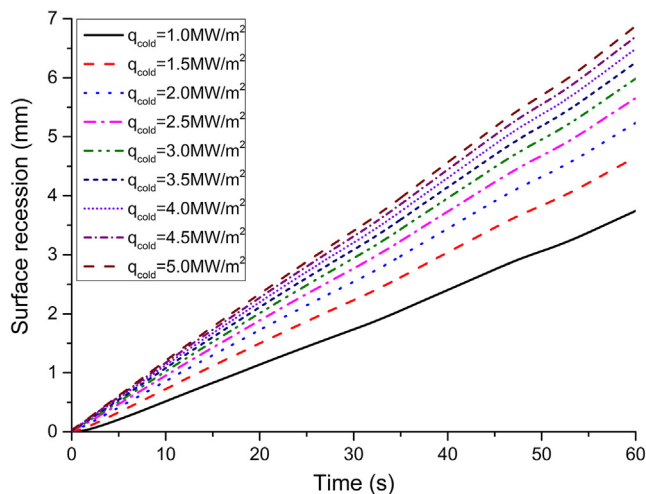


Fig. 8. Comparison of surface recession from cold wall heat flux.

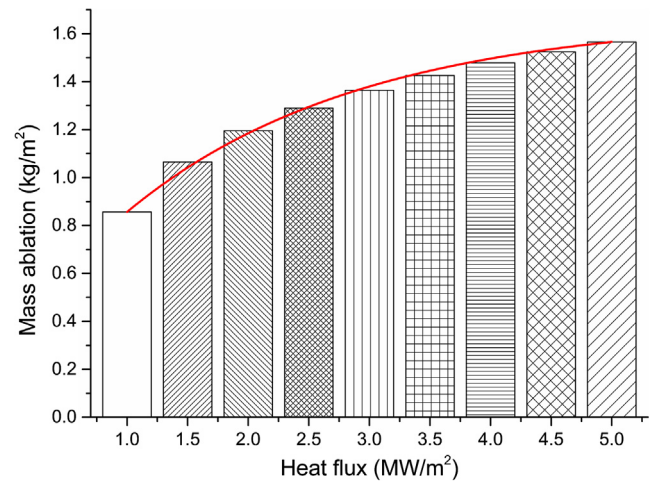


Fig. 9. Comparison of mass ablation per area from cold wall heat flux.

face recession becomes more and more weak. Meanwhile, the comparison of mass ablation per area from cold wall heat flux is also shown in Fig. 9. The mass ablation per area is respectively 0.85672 kg/m², 1.06482 kg/m², 1.19531 kg/m², 1.28996 kg/m²,

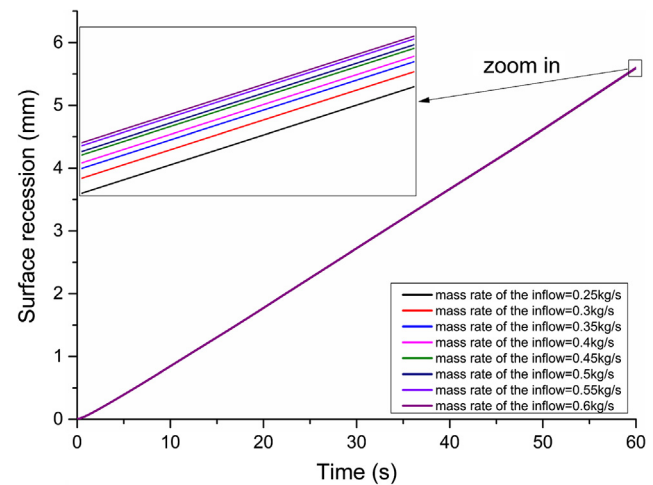


Fig. 10. Comparison of surface recession from mass rate of the inflow.

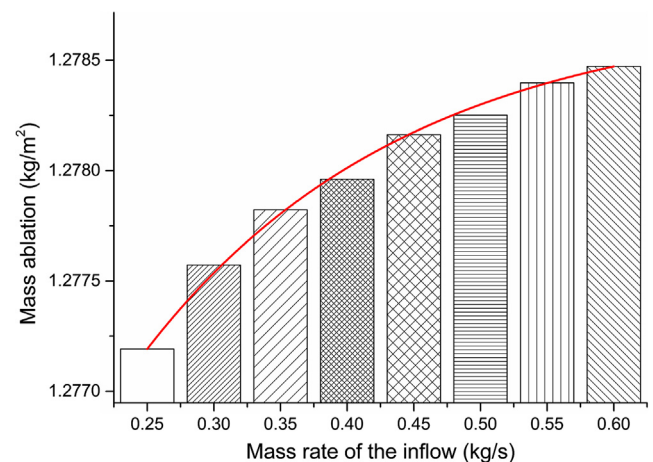


Fig. 11. Comparison of mass ablation per area from mass rate of the inflow.

1.36442 kg/m², 1.42606 kg/m², 1.47880 kg/m², 1.52496 kg/m² and 1.56605 kg/m² corresponding to each heat flux. With the increasing of the heat flux, the rising rate of the mass ablation per area is respectively 19.54%, 10.92%, 7.34%, 5.46%, 4.32%, 3.57%, 3.03% and 2.62%. It is also a validation of that the increasing rate of the surface recession becomes more and more weak with the rising of heat flux.

Figs. 10 and 11 show the influence on surface ablation from the mass rate of the inflow. Fig. 10 compares the surface recession when the mass rate changes from 0.25 kg/s to 0.6 kg/s. Due to that the surface recession curve is too close to each other and cannot be distinguished, an enlarged drawing of the ending part of each curve is also given. With the rising of the mass rate of the inflow, the surface recession increases slightly. Fig. 11 gives the relationship between the mass ablation per area with the increasing mass rate, which also shows that with the increasing mass rate, the surface ablation aggravates with a weak rising. Moreover, the increasing rate of the mass ablation gets smaller when the mass rate becomes larger. It is obvious that the amount of oxidative gases under the large mass rate is higher than that under the small mass rate. In spite of there are reactions happened in the boundary layer, the consuming of the oxidative gases is restricted. Thus, the resident oxidative gases from under large mass rate are higher than that under small mass rate, which leads the surface ablation seriously when the mass rate of the inflow is larger.

5. Conclusions

A coupled method to determine the surface ablation rate of charring materials for vehicles during reentry is proposed in this paper. The results are compared to the experimental data to show a validation in forecasting the surface ablation of charring materials. The numerical results show that

- By comparing to the experimental data, the coupled method is validated to be effective to solve the surface ablation of charring materials.
- The coupled method can more accurately predict the surface recession than the uncoupled method, because that some parameters in the inflow, such as the cold wall heat flux and the mass rate, have influence on the surface ablation.

Acknowledgments

This work was supported by the National Natural Science Foundation of China (11472037, 11272042 and 51506008).

References

- T. Cheng, W. Li, W. Lu, Heat transfer and failure mode analyses of ultrahigh-temperature ceramic thermal protection system of hypersonic vehicles, *Math. Probl. Eng.* 2014 (13–14) (2014) 1–11.
- S.L. Guo, B.L. Wang, C. Zhang, Thermal shock fracture mechanics of a cracked solid based on the dual-phase-lag heat conduction theory considering inertia effect, *Theor. Appl. Fract. Mech.* 86 (2016) 309–316.
- J.M. Park, D.J. Kwon, Z.J. Wang, Effects of carbon nanotubes and carbon fiber reinforcements on thermal conductivity and ablation properties of carbon/phenolic composites, *Compos. Part B-Eng.* 67 (2014) 22–29.
- S.S. Pawar, V.P. Vavilov, Applying the heat conduction-based 3D normalization and thermal tomography to pulsed infrared thermography for defect characterization in composite materials, *Int. J. Heat Mass Trans.* 94 (2016) 56–65.
- S.L. Guo, B.L. Wang, Thermal shock cracking behavior of a cylinder specimen with an internal penny-shaped crack based on non-fourier heat conduction, *Int. J. Thermophys.* 37 (2) (2016) 1–23.
- Q. Liu, Y. Wang, J. Lei, Numerical investigation of the thermophysical characteristics of the mid-and-low temperature solar receiver/reactor for hydrogen production, *Int. J. Heat Mass Trans.* 97 (2016) 379–390.
- W.J. Li, H.M. Huang, Y. Tian, A nonlinear pyrolysis layer model for analyzing thermal behavior of charring ablator, *Int. J. Therm. Sci.* 98 (2015) 104–112.
- W.J. Li, H.M. Huang, Y. Tian, Nonlinear analysis on thermal behavior of charring materials with surface ablation, *Int. J. Heat Mass Trans.* 84 (2015) 245–252.
- W.J. Li, H.M. Huang, B.C. Ai, On the novel designs of charring composites for thermal protection application in reentry vehicles, *Appl. Therm. Eng.* 93 (2016) 849–855.
- B. Aghaaliakbari, A.J. Jaid, M.A.A. Zeinali, Computational simulation of ablation phenomena in glass-filled phenolic composites, *Iran J. Chem. Chem. Eng.* 34 (1) (2015) 97–106.
- H. Weng, S.C.C. Bailey, A. Martin, Numerical study of iso-Q sample geometric effects on charring ablative materials, *Int. J. Heat Mass Trans.* 80 (2015) 570–596.
- J. Scoggins, N. Mansour, H. Hassan, Development of reduced kinetic mechanism for pica pyrolysis products, in: 42nd AIAA Thermophysics Conference, Honolulu, Hawaii, 2011, AIAA 2011-3126.
- J. Scoggins, H. Hassan, Pyrolysis mechanism of PICA, in: 10th AIAA/ASME Joint Thermophysics and Heat Transfer Conference, Chicago, Illinois, 2010, AIAA 2010-4655.
- H.W. Wong, J. Peck, J. Assif, Quantitative determination of species production from the pyrolysis of the Phenolic Impregnated Carbon Ablator (PICA), in: 53rd AIAA Aerospace Sciences Meeting Kissimmee, Florida, 2015, AIAA 2015-1447.
- J.B. Scoggins, Development of mutation++: multicomponent thermodynamic and transport properties for ionized plasmas written in C++, in: 11th AIAA/ASME Joint Thermophysics and Heat Transfer Conference, Atlanta, GA, AIAA 2014-2966, 2014.
- D.R. Olander, W. Siekhaus, R. Jones, Reactions of modulated molecular beams with pyrolytic graphite. I. Oxidation of the basal plane, *J. Chem. Phys.* 57 (1) (1972) 408–420.
- H.D. Allendorf, D.E. Rosner, High-temperature kinetics of graphite oxidation by dissociated oxygen, *AIAA J.* 3 (8) (1971) 1522–1523.
- B. Mccarroll, D.W. Mckee, Reactivity of graphite surfaces with atoms and molecules of hydrogen, oxygen, and nitrogen, *Carbon* 10 (3) (1971) 301–311.
- J. Keenan, Simulation of graphite sublimation and oxidation under re-entry conditions, in: 6th Joint Thermophysics and Heat Transfer Conference Colorado Springs, CO, 1994, 1994-2083.
- R.L. Baker, Graphite ablation chemistry nonequilibrium effects, in: 10th Thermophysics Conference, Los Angeles, Calif, 1975-735, 1975.
- C. Park, Calculation of stagnation-point heating rates associated with stardust vehicle, *J. Spacecraft Rockets* 44 (1) (2006) 24–32.
- F.S. Milos, Y.K. Chen, T. Gokcen, Nonequilibrium ablation of phenolic impregnated carbon ablator, *J. Spacecraft Rockets* 49 (5) (2013) 894–904.
- S.M. Scala, Entry Heat Transfer and Material Response, Re-Entry and Planetary Entry Physics and Technology, Applied Physics and Engineering, vol. 2, Springer, Berlin, Heidelberg, New York, 1968, pp. 436–487.
- H.G. Maahs, Oxidation of carbon at high temperatures: Reaction-rate control or transport control, NASA Technical Note, NASA TN D-6310, 1971.
- C.B. Moyer, R.A. Rindal, An analysis of the coupled chemically reacting boundary layer and charring ablator, Part II: Finite difference solution for the in-depth response of charring materials considering surface chemical and energy balances, NASA Contractor Report, NASA CR-1061, 1968.
- D.M. Curry, An analysis of a charring ablation thermal protection system, NASA Technical Report, NASA TN D-3150, 1965.
- P.A. Gnoffo, R.N. Gupta, J.L. Shinn, Conservation equations and physical models for hypersonic air flows in thermal and chemical non-equilibrium, NASA Technical Paper, 1989, NASA TR N-89.
- P.A. Gnoffo, McCandless, Enhancements to program LAURA for computation of three-dimensional hypersonic flow, in: 25th AIAA Aerospace Sciences Meeting, Reno, NV, 1987, AIAA 1987-280.
- A. Ballter-Peterson, F. Nichols, B. Mifsud, Arc jet testing in NASA Ames Research Center thermophysics facilities, in: AIAA Materials Specialist Conference - Coating Technology for Aerospace Systems. 4th Symposium on Multidisciplinary Analysis and Optimization Cleveland, OH, AIAA 1992-5041, 1992.
- F.S. Milos, Y.K. Chen, Ablation and thermal response property model validation for phenolic impregnated carbon ablator, *J. Spacecraft Rockets* 47 (5) (2010) 786–805.
- T. Gokcen, Y.K. Chen, K.A. Skokova, Computational analysis of arc-jet stagnation tests including ablation and shape change, *J. Thermophys. Heat Transf.* 24 (4) (2012) 694–707.
- W.J. Li, H.M. Huang, Q. Wang, Protection of pyrolysis gases combustion against charring materials' surface ablation, *Int. J. Heat Mass Transf.* 102 (2016) 10–17.
- W.J. Li, H.M. Huang, X.L. Xu, A new mechanism of surface ablation of charring materials for a vehicle during reentry, *Appl. Therm. Eng.* 106 (2016) 838–849.
- B.Y. Lattimer, J. Ouellette, J. Trelles, Thermal response of composite materials to elevated temperatures, *Fire Technol.* 47 (4) (2011) 823–850.
- S. Srinivasan, J.C. Tannehill, K.J. Weilmuenster, Simplified curve fits for the thermodynamic properties of equilibrium air, NASA Technical Report, NASA-RP-1181, 1987.
- M. Sobera, J. Hetper, Pyrolysis-gas chromatography-mass spectrometry of cured phenolic resins, *J. Chromatogr. A* 993 (1–2) (2003) 131–135.
- K.A. Trick, T.E. Saliba, Mechanisms of the pyrolysis of phenolic resin in a carbon/phenolic composite, *Carbon* 33 (11) (1995) 1509–1515.
- R.J. Kee, J.A. Miller, G.H. Evans, A computational model of the structure and extinction of strained, opposed flow, premixed methane-air flames, *Symp. Combust.* 22 (1989) 1479–1494.

- [39] C.Y. Wen, H.G. Hornung, Non-equilibrium dissociating flow over spheres, *J. Fluid Mech.* 299 (1995) 389–405.
- [40] C. Park, Effects of atomic oxygen on graphite ablation, *AIAA J.* 14 (11) (1976) 1640–1642.
- [41] H.K. Tran, C.E. Johnson, D.J. Rasky, Phenolic Impregnated Carbon Ablators (PICA) as thermal protection systems for discovery class missions, in: 31st Thermophysics Conference New Orleans, LA, 1996, 1996–1911.
- [42] J.B. Henderson, J.A. Wiebelt, M.R. Tant, A model for the thermal response of polymer composite materials with experimental verification, *J. Compos. Mater.* 19 (6) (1985) 579–595.
- [43] S.D. Williams, D.M. Curry, Thermal protection materials: Thermophysical property data, NASA Technical Report N, 1992, NASA RP 1289.
- [44] A.D. Bianco, D. D'Ambrosio, V. Mareschi, A fully implicit material response code with ablation and pyrolysis for simulation of thermal protection systems, in: 8th European Symposium on Aerothermodynamics for Space Vehicles, At Lisbon, Portugal, 2015, pp. 87–122.
- [45] D.M. Curry, E.W. Stephens, Apollo ablator thermal performance at superorbital entry velocities, NASA Technical Note, 1970, NASA TN D-5969.
- [46] B. Serauskas, S. Gerg, M. Frenklach, <<http://combustion.berkeley.edu/grimech/index.html>>.